UC Berkeley
UC Berkeley Previously Published Works

Title

CsI(Na) Detector Array Characterization for ARES Program

Permalink

Journal

ISSN

Authors

Quiter, Brian J
Joshi, Tenzing HY
Bandstra, Mark S
et al.

Publication Date

2016-04-01

DOI

CsI(Na) Detector Array Characterization for ARES Program

Brian J. Quiter, Tenzing H. Y. Joshi, Mark S. Bandstra, and Kai Vetter

Abstract—Researchers at Lawrence Berkeley National Laboratory have been supporting the Transformational and Applied Research Directorate in the Domestic Nuclear Detection Office of the Department of Homeland Security to define needs for, to develop, and to test a scintillator-based radiation detection and localization system to be fielded on a helicopter platform - the so-called Airborne Radiological Enhanced-sensor System. The system comprises an array of 92 CsI(Na) detectors that are arranged to function as an active mask to encode the directionality in the roll-dimension of measured gamma rays and is additionally capable of Compton imaging. Additional contextual sensors and specially-developed algorithms are also being fielded for characterization with the goal of detecting, localizing, and helping to interdict radiological and nuclear threats via airborne search. The algorithms that are being developed leverage contextual information including topography, geography, hyperspectral imagery, video tracking, and platform positioning. This paper describes recent characterization efforts of the CsI(Na) detector system including energy, position, and timing resolution and synchronization between the 184 individual photomultiplier tubes.

Index Terms—Gamma-ray detectors, position sensitive particle detectors, solid scintillation detectors, radiation imaging, security applications.

I. INTRODUCTION

THE desire for effective radiological source detection and localization capabilities has motivated the U.S. Department of Homeland Security to support research and development towards advancing airborne radiation detection capabilities. The Transformational and Applied Research Directorate in the Domestic Nuclear Detection Office (DNDO) started the Airborne Radiological Enhanced-sensor System (ARES) Advanced Technology Demonstration in FY2013 and has now taken delivery of the sensor system, which is highlighted by 92 CsI(Na) radiation detector crystals based on previous designs [1]. Additionally, there are contextual sensors including a global position unit/inertial navigation system

(GPU/INS), a radar altimeter, a video camera array for vehicle tracking, and a weather sensor. Algorithms being developed for the ARES program take data produced by these sensors along with additional contextual information provided by a database describing terrain, topography, buildings, and materials to produce detection, localization and identification outputs with the goal of achieving significant improvements in the ability of an airborne system to detect, localize and track radiological and nuclear threats and to highlight which sensor components, contextual data, and algorithms are of most value for improving airborne radiation detection capabilities.

The γ-ray detectors are small aspect ratio (1"x 1"x16.5") CsI(Na) bars attached via light guides on each end to photomultiplier tubes (PMTs) and otherwise encapsulated in light-tight aluminum housings. The detectors are grouped into two pairs of arrays, each with 23 detectors that are arranged to enable photon source localization via active coded mask and/or Compton imaging. A schematic description of the detector arrangement is shown in Fig. 1, along with reconstructed positron annihilation rays that indicate the position resolution of the system and demonstrate timing synchronization. Two aluminum pods, mounted external to the helicopter, each carry two detector arrays.

A measured γ ray may be localized along the dimension of the long axis of the detector volume, x, by comparing the relative signal intensities observed in the two PMTs attached to each crystal. This localization, in turn can be used to improve the effective energy resolution. In the following, characterization methods are described including assessments of position and energy determination and system synchronization. The new event reconstruction method described here is similar, but different to methods that have been previously developed elsewhere (such as [2]), and are compared to a more direct method that can be considered a default event reconstruction method.

II. MEASURED EVENT RECONSTRUCTION

Scintillation light in the CsI(Na) crystals is converted to electronic signals using Hammamatsu R3998-02 PMTs. These signals are fed to 8-channel, 14-bit, 100MS/s CAEN Digital Pulse Height Analyzers (DPHAs). Event reconstruction requires that the pair of PMTs located on opposite ends of a CsI(Na) crystal produce signals whose integrated intensity exceed a predefined software threshold and are within 80 ns of one another. When a PMT event is unpaired, it is flagged and excluded from future analysis for all purposes except estimating detector deadtime. Example pulse height spectra from a typical flight are shown in Fig. 2. Histograms of paired event amplitudes are
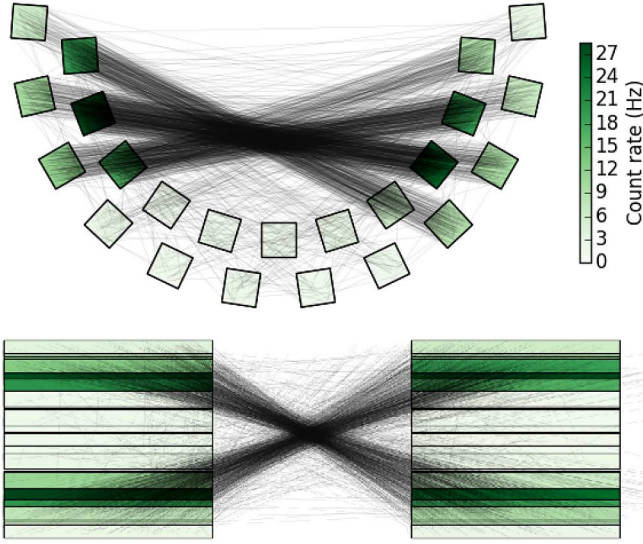
Fig. 1. Two schematic views (top is end-on, bottom is top-view) of the CsI(Na) bar positions in a 23 detector array (top) or a pair of arrays (bottom). The CsI(Na) bars are shown in green and rays connecting positions between bars indicate a measured pair of coincident events within the 511 keV peak regions, as described in Section IV. The highest concentrations of rays corresponds to the approximate position of the ^{22}Na source. The scale indicates the number of measured coincident events in each crystal.
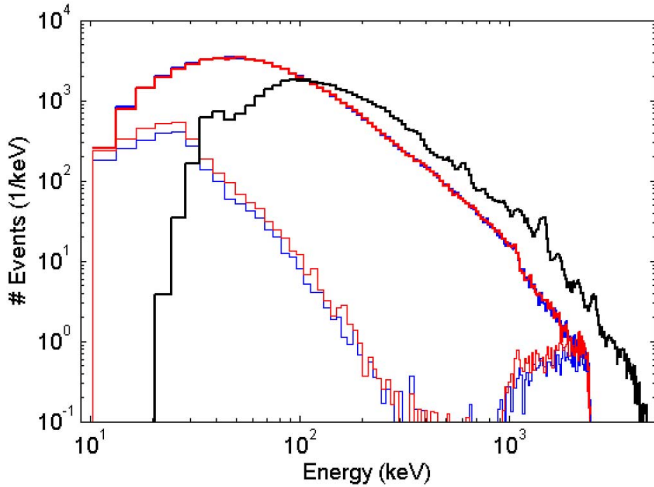

Fig. 2. Example PMT energy spectra for a single CsI(Na) crystal (color online). Heavy lines correspond to paired events, light lines to unpaired events. Red and blue correspond to PMT 1 and 2, respectively. The heavy black histogram is due to the summation of the paired event energies. The 1460-keV peak was used to produce an approximate position-independent linear energy calibration.

shown as the heavy red and blue lines, the unpaired spectra for the corresponding PMTs are shown as the lighter lines. The maximum integrated pulse amplitude allowed by the dynamic range of the DPHA is also visible, indicated by the cutoff for the single PMT spectra at approximately 2.65 MeV; the summed energy associated with such an event that also had a pair would be higher, as is more apparent in Fig. 4, below. The paired event summed spectrum is shown as the black line and the evident peak at 1460 keV was used as an approximate energy calibration. More advanced methods to reconstruct energy and position of the paired events are described in the following.
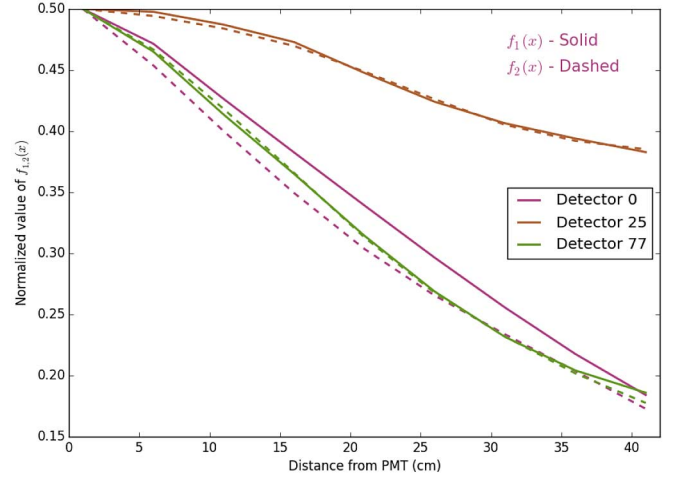

Fig. 3. Example of functions $f_{1,2}(x)$ for detectors 0, 25, and 77. These three detector exhibit some of the behavior observed in the 92 ARES detectors. All of the detectors exhibit non-exponential behavior. Detector 0 exhibits asymmetric light transport which is accounted for in the new calibration approach. Detector 25 exhibits very little attenuation, which results in poor position resolution and detector 77 has desirable symmetry and attenuation.

A. Theory

An idealized method to reconstruct the one dimensional position and event energy within a scintillator that is read out with PMTs on opposite faces has been derived elsewhere [3]. This approach predicts the magnitudes of signals read out by the PMTs as

$$E_1 = E_\gamma \frac{p}{E_0} \exp[-\alpha(L/2 - x)], \tag{1}$$

$$E_2 = E_\gamma \frac{p}{E_0} \exp[-\alpha(L/2 + x)]. \tag{2}$$

Here $E_{1,2}$ is the DPHA readout of each PMT, E_γ is the amount of energy deposited at position x, relative to the center, in a scintillator of length L, α is the light loss per unit length, E_0 is the scintillation efficiency of the scintillator, and p is phototube sensitivity. This approach makes several assumptions, including: (1) light loss through the scintillator is uniform, meaning the amount of light collected from an event decreases exponentially with distance from the PMT, (2) the gain of the PMTs are matched ($p_1 = p_2$) and linear, and (3) the energy deposition is point-like in space. These assumptions yield analytic solutions for energy and position that are independent of one another

$$E_\gamma = \frac{E_0}{p} \exp(\alpha L/2) \sqrt{E_1 E_2} \tag{3}$$

$$x = \frac{1}{2\alpha} \log \frac{E_2}{E_1}. \tag{4}$$

Care must be taken in the application of this approach due to the sensitivity of E_0 and p to temperature, the former causing gain drift and the later causing drift in both energy and position.

Unfortunately, this approach should not be directly applied to the ARES detector system. Calibration data shows a non-uniform light loss across the detectors (Fig. 3), and light-collection has been observed to change over time, resulting

in unmatched PMT gains, which may further vary due to harsh environmental conditions including variation in temperature, vibrations, and shocks. To generate a robust and easily correctable calibration, a more general relationship between measured PMT signal and energy deposition is assumed

$$E_1 = E_\gamma \frac{p_1}{E_0} f_1(x) = E_\gamma P_1 f_1(x) \quad (5)$$

$$E_2 = E_\gamma \frac{p_2}{E_0} f_2(x) = E_\gamma P_2 f_2(x). \quad (6)$$

This generalization defines the light collection efficiency as an arbitrary function of position $f_{1,2}(x)$, and leaves the gain of each PMT ($p_{1,2}$) as independent and, for now, assumes a linear PMT response. Fluctuations in E_0 are not expected to show position dependence within a detector. As a result, E_0 acts as a scaling factor for $p_{1,2}$. For simplicity we combine these terms into $P_{1,2}$. The functions, $f_{1,2}(x)$ may be characterized with a series of calibration measurements taken at incremental locations along the length of the scintillator with a collimated γ-ray source. The constants $P_{1,2}$ can then be calculated knowing the energy of the calibration γ rays. We define the convention of $f_{1,2}(x_0) = 0.5$ where x_0 is the calibration position nearest the respective PMTs. Additionally, once $f_{1,2}(x)$ are characterized they are assumed to remain unchanged even as gains change.[1] This leaves only $P_{1,2}$ and any non-linear energy effects to be re-calibrated should drift occur.

B. Calibration Data

The CsI(Na) detectors were calibrated using a fan-beam collimated ^{137}Cs source that concurrently irradiated all 23 detectors within an array. Calibration data was acquired at nine positions in 5 cm increments from 1–41 cm along each of the 42 cm detectors. The signals were integrated and recorded from both PMTs ($E_{1,2}$), and data was processed to select the 662 keV photo peak events. The location of the peaks (in $E_{1,2}$) was recorded for all nine positions and normalized per convention. These normalized points were used to produce spline fits defining $f_{1,2}(x)$, where a quadratic spline was applied for $1 > x > 41$ and linear extrapolation was applied outside of this region. The values of $P_{1,2}$ were calculated during the normalization process, given the known energy of the ^{137}Cs photo-peak, and are used as the initial guess for subsequent calibration.

C. Solving for Position and Energy

To calculate event location in terms of $E_{1,2}$, we invert the relationship of $f_{1,2}(x)$ and $P_{1,2}$

$$L(x) = \frac{P_1 f_1(x)}{P_2 f_2(x)} = \frac{E_1}{E_2}. \quad (7)$$

The function $L^{-1}(E_1/E_2)$ is defined as a quadratic spline within the detector calibration and a linear extrapolation outside of this region, using evaluations of the characterized functions $f_{1,2}$ and the measured values of $P_{1,2}$.

[1]Operational experience indicates that this assumption has proven sufficiently valid as the performance of the calibration method has remained fairly constant over $\sim$100 hours of system operation across more than six months.

The energy can then be calculated using the reconstructed position and the relationship

$$E_\gamma = \frac{(E_1 + E_2)/C}{P_1 f_1(x) + P_2 f_2(x)} = \frac{E_1 + E_2}{P_1' f_1(x) + P_2' f_2(x)} \quad (8)$$

where C is a proportional scaling of $P_{1,2}$ that is calculated via energy calibration. This relationship, however, lacks inclusion of any non-linearity in system response. During characterization of the ARES system, non-linearity of the detectors has been measured to be $\epsilon \sim \mathcal{O}(10^{-5})$. As a result, this non-linearity is insignificant for position calibration, but appreciable for energy calibration. We therefore include a non-linear term ϵ that is proportional to the total amplitude of the corrected energy signal

$$E_\gamma' = E_\gamma(1 + \epsilon E_\gamma). \quad (9)$$

The values of C and ϵ are determined independently in post-processing by analyzing the positions of known photo-peaks such as those at 609, 1460, and 2615 keV from background measurements.

D. Recalibration of $P_{1,2}$

While $f_{1,2}$ are expected to be intrinsic properties of each detector crystal and its readout assembly, P_1/P_2 and C ($i.e. P_{1,2}'$) define the PMT sensitivity and scintillation efficiency of the crystal, and are expected to vary with measurement conditions. The assumption of uniform irradiation that results from typical large stand-off scenarios enables values of P_1/P_2, to be determined for each measurement.

The ratio P_1/P_2 is determined by iteratively minimizing the number of events that would be reconstructed outside of the detector volume. The Nelder-Mead minimization routine was selected to perform the minimization [4]. During each iteration, the function $L^{-1}(E_1/E_2)$ is recalculated and the position of each event then recalculated using L^{-1}. A weighted sum

$$\sum_i \frac{1}{2} \left[1 - \mathrm{erf} \frac{|x_i| - 21}{1.6\sqrt{2}} \right] \quad (10)$$

is used as the minimizing parameter, where x_i is the position of the ith event. The constant, 1.6 cm was selected based on the observation of the mean position resolution at detector edges, as indicated in Fig. 6. The minimization weighting represents the fact that with finite position resolution, some events are expected to be reconstructed a small distance outside of the physical dimension of the detector volume, and facilitates convergence to physical solutions; the selection of an error function to weight the minimization would result in the best performance if position observations were normally distributed about the true locations. This process finds the value of P_1/P_2 that maximizes the number of events that are reconstructed within physical positions ($|x_i| < 21$). After this process, uncalibrated values of each E_γ are calculated for $C = 1$ and the 609, 1460, 2615 keV background peaks are fit. The values of C and ϵ are then determined by fitting known peak energies and Equations (8) and (9).

E. Comparison with Polynomial Fits

A more direct approach to event reconstruction would be to use the quantity $E' = E_1 + E_2$ to represent energy deposition and $x' = (E_1 - E_2)/(E_1 + E_2)$ to represent the interaction position. Using the same calibration data as described in Section II-B, third-order and fifth-order polynomials, $x = p(x')$ and $E = p_2(E')$, are fit to serve as calibrated mappings between measurement and reconstructed position and energy, respectively. Linear fits would be equivalent to a first-order Taylor expansion to Equations (3) and (4). Subsequent to calibration, each measured event is reconstructed using the fit polynomials. Similar to the previous reconstruction method, an additional linear energy scaling was found to be necessary, which was applied after data collection and derived from known background lines. The drawback of this method is that the position reconstruction is fixed and relative fluctuations between PMTs result in reconstructed energies that can have position-dependent biases, resulting in worse energy resolution characteristics than would be expected from spectra derived from interactions within a thin slice of detectors' volume.

Fig. 4 shows a comparison of calibrated background data using the approach described within this paper and the simpler polynomial approach. The data in Fig. 4 was taken six months and ~ 100 hours of operation after the acquisition of the calibration data used to determine $f_{1,2}(x)$, $p(x')$ and $p_2(E')$. The calibration method presented here improves both the number of events successfully reconstructed with the physical dimensions of the detectors and the energy resolution of the system. The root-mean-square resolution of the 1460 keV peak is found to be 31.1 keV, using the new calibration method, compared with 34.0 keV using the direct polynomial fit method. A comparison of the energy resolution for each detector is provided as Fig. 5.

III. POSITION PERFORMANCE

As mentioned above, interaction positions within a detector volume are estimated by comparing the intensities of the signals produced by the PMT pair on opposite ends of a crystal. Directly measuring the position reconstruction performance of the system while in flight is not a trivial tasks because practical considerations preclude placement of a collimated source within a detector array while flying, and land-based sources result in nearly uniform irradiation when measured at standoff distances achievable while in flight. Instead, we present descriptions of three less direct assessments of the position performance: one that analyzes the laboratory-collected collimated calibration data using a ^{137}Cs source; a second derived from the position distribution of events that are reconstructed near the edge of a crystal; and a third that examines the position response when the detectors are irradiated near-uniformly. The first method gives some indication of the position uncertainty associated with the statistical limitations from limited light collection as propagated through the event reconstruction formalism, the second presents direct measures of the position resolution at the edges of the detector, and the third provides some assessment of true inaccuracies that result from the position reconstruction method.
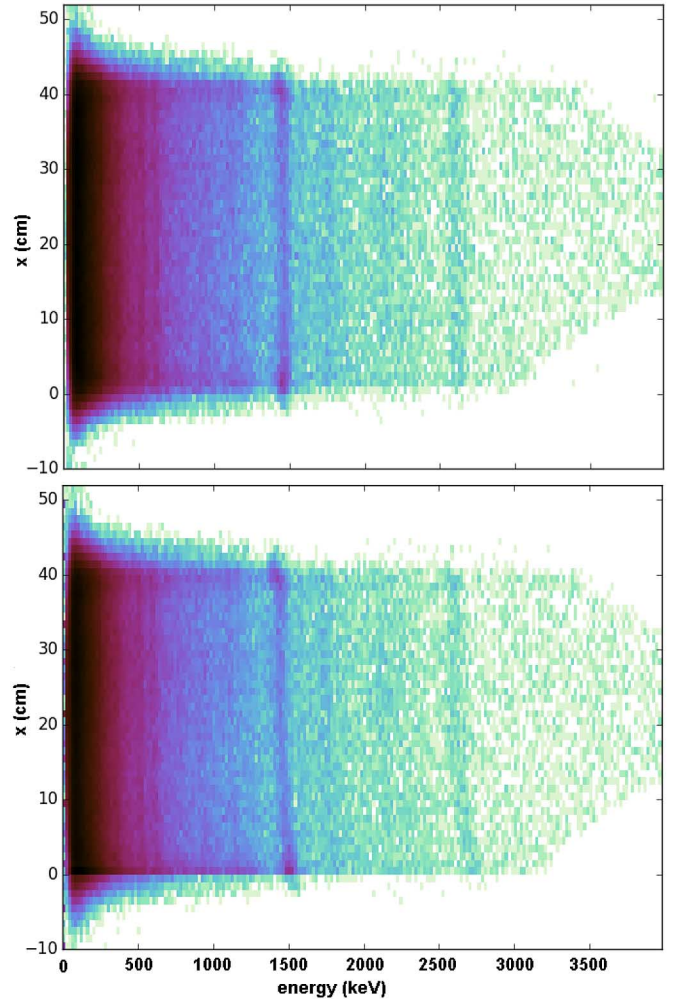

Fig. 4. Comparison of two-dimensional histograms of reconstructed energies and positions for a single detector measuring background. The top distribution was generated using the reconstruction method described here and the bottom is from the more direct reconstruction approach described in Section II-E.

The calibration data used to define $f_{1,2}(x)$ were fit, obtaining values of $E_{1,2}$ and the associated widths of the peaks, $\sigma_{E_{1,2}}$. The spline-interpolated function, $L(x)$ from Equation (7) is inverted and the associated position uncertainty is given by

$$\sigma_x = \frac{dx}{d(L^{-1}(E_1/E_2))} \frac{E_1}{E_2} \sqrt{(\sigma_{E_1}/E_1)^2 + (\sigma_{E_2}/E_2)^2} \quad (11)$$

where $\sigma_{E_{1,2}}$ are obtained from the calibration data and $E_1/E_2 \sqrt{(\sigma_{E_1}/E_1)^2 + (\sigma_{E_2}/E_2)^2}$ is also spline-interpolated. The resulting estimate of position resolution is shown in Fig. 6, which would be a reasonable estimate at 662 keV based on the calibration data, but similar data at other energies is unavailable. The positioning behavior near the edge of the crystal can also be used to more directly assess the true position resolution while in flight.

Position histograms resulting from the event reconstruction procedure are shown in Fig. 7. Histograms for all event energies, as well as within energy ranges of 580–740 keV and 1800–2700 keV are shown. There tends to be a fairly flat region within the crystal dimension and tailing extending beyond each
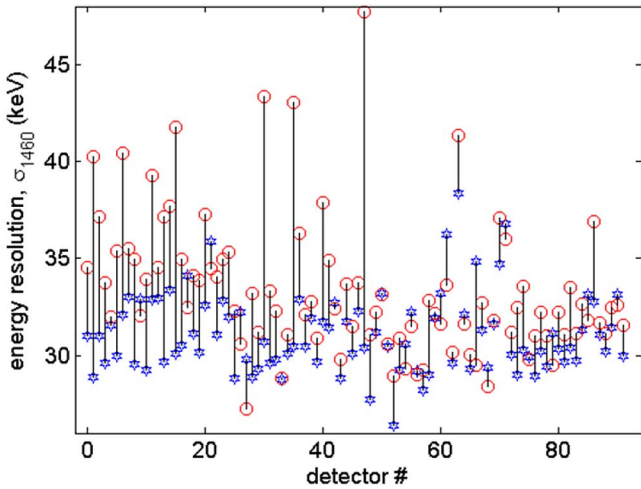
Fig. 5. Comparison of fit energy resolutions at 1460 keV in background spectra using the new approach and the polynomial fit for each detector. The red circles correspond to the simplified approach and the blue stars to the generalized light-loss function described herein. Lines connecting the two data points are to help guide the eye.
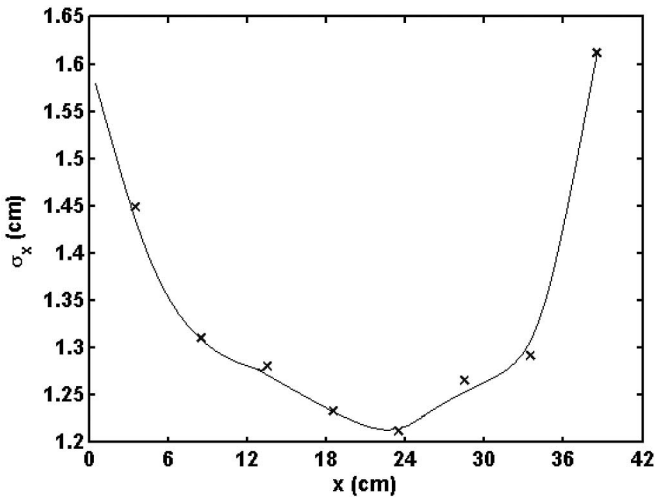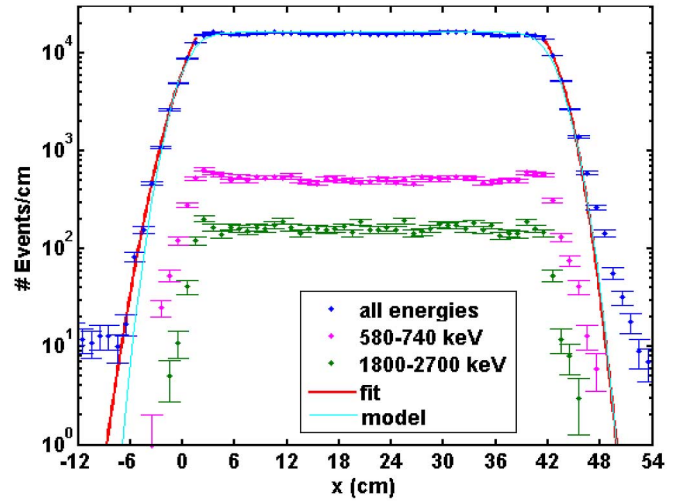

Fig. 7. Position histogram for all events from a single detector with fit functions near the crystal ends (blue with error bars due to counting statistics) and for the energy ranges of 580–740 keV (magenta) and 1800–2700 keV (green). The data from all energies were fit (red), as described in the text. This detector's fit σ_F values are 2.1 and 1.7 cm for the left and right ends, respectively. Also shown (cyan) is a model distribution where a flat-top distribution is convolved with a Gaussian distribution of width, 1.9 cm.

Fig. 6. Averaged position resolution, σ_x, obtained from Equation (11) using the characterization data of the 85 detectors that demonstrated typical performance.

end. The tailing was fit as a flat-top function for $x \in [0, 42]$ convolved with a Gaussian function of variable width, σ_F. The best fit values of σ_F are quite comparable to those anticipated from the calibration data. The median value of σ_F at the detector ends, determined from this fitting method was 1.9 cm when all energies were considered. The fitted values typically ranged from 1.4 to 3.5 cm, but four detectors appear to have particularly poor position resolution, and their σ_F values extended up to 9.5 cm. This estimate of position resolution appears to be worse than that obtained from analyzing the Poisson statistics associated with the calibration data. However, the calibration data was generated for 662 keV γ rays. Performing the same analysis for events ranging from 580–740 keV produce a mean σ_F value (omitting the four outliers) of 1.5 cm, which is very close to the position resolution at the crystal edge expected from the calibration data. For the 1800–2700 keV energy range, mean σ_F value is 1.2 cm. These values are approaching the

expected positional uncertainty in the dimensions perpendicular to the crystal axis just due to the crystals' size.

The data shown in Fig. 7 also demonstrate some systematic variations that appear to be inconsistent with the assumption of uniform irradiation, particularly at lower energies, where there is higher statistical confidence. The position reconstruction biases appear at inflection points in the fitted calibration functions, typically near the crystal edges. Qualitatively, it is clear that the reconstruction preferentially produces certain positions and the scale of this bias appears to be up to a few centimeters.

IV. CROSS-ARRAY SYNCHRONIZATION

Two methods of demonstrating synchronization across a detector array (and between adjacent arrays) have been pursued. In the first, a ^{22}Na source is positioned either within an array or between adjacent arrays. By drawing rays between positions reporting coincident 511 keV energy depositions, an image of the approximate source position can be constructed. The images shown in Fig. 1 are examples of this. Both were obtained using a 2.2 μCi source of ^{22}Na and 2,000 coincident events have been drawn. The terminus of the rays within each detector were taken from the nominal positions that resulted from the $E_1 - E_2/E_1 + E_2$ position determination method along the crystal axis and were randomly selected from a uniform distribution along the other dimensions.

The spectra of the events that are identified as non-coincident and those identified as coincident further confirm the synchronization of the system. Fig. 8 shows the entire spectrum resulting from the reconstruction method described here and, using a 160 ns time window for coincident events within a pod (i.e., within the two co-located arrays). The relative amplitudes of the non-coincident (singles) and coincident spectra are within expectation from Monte Carlo modeling. The 160 ns
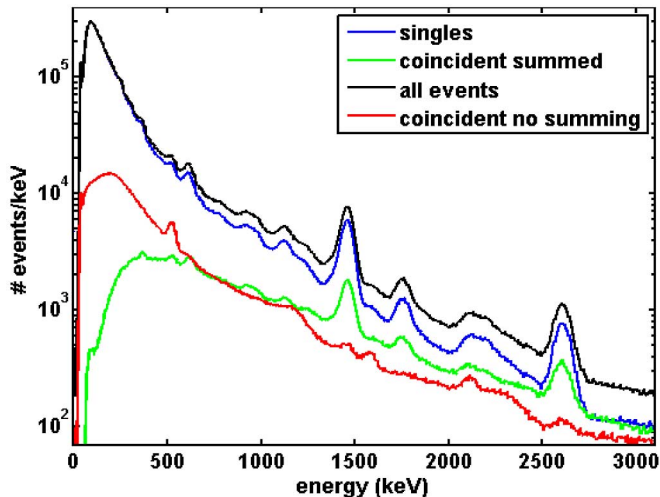
Fig. 8. Energy spectra from a single flight for events identified as non-coincident (blue), coincident (green), and the sum (black). The spectrum of the individual coincident energy depositions is also shown (red). There are a total of 5.6 million singles and 3 million coincident events, 580,000 of which are sequences corresponding to three or more interactions.

window was selected because the system digitizes the times of events with 80 ns precision and a two-bin wide window was found to encompass all coincident events. This digitization precision essentially dictates the timing resolution of the system, rather than the scintillation properties of the NaI(Tl). Also of note is the presence of spectral features in the histogram of the coincident event energies prior to summing. These show very prominent Compton edges, escape peaks, and annihilation peaks and almost no full-energy peaks. This is what is to be expected from a spectrum of truly coincident events, whereas chance coincidence events would contribute disproportionately to the full-energy peaks within the spectrum.

V. CONCLUSION

Characterization of the performance of the ARES detector array has been accomplished. PMT and cross-array synchronization has been demonstrated and a new method that improves the determination of energy depositions within detectors has been developed and tested. Interaction positions that are determined using this new method show comparable statistically-driven position uncertainties, but show smaller systematic errors, likely due to improved stability of the reconstruction method with gain drift. Along with a well-synchronized system, the improved energy and position determination will likely improve the contribution of Compton imaging toward localizing point-like radiological source in search scenarios. Modeling and data analysis to demonstrate the Compton imaging performance of the system and to quantify the Compton imaging performance improvement due to application of the event reconstruction method described here are the subject of future work.

Additionally, the final characterization stage of the ARES ATD has recently begun. More in-depth analyses of the active mask imaging capabilities of the system; and the impacts of other contextual sensors, topography and materials databases, and more advanced detection algorithms will be assessed with respect to the goals of demonstrating improved system performance in radiological threat source detection and localization from an airborne platform. The improved energy resolution demonstrated herein will likely contribute to improved performance throughout the ARES system.

REFERENCES

[1] R. D. Penny *et al.*, "A dual-sided coded-aperture radiation detection system," *Nucl. Instrum. Meth. Phys. Res. A*, vol. 652, no. 1, pp. 578–581, 2011.
[2] A. M. L. MacLeod, P. J. Boyle, D. S. Hanna, P. R. B. Saull, L. E. Sinclair, and H. C. J. Seywerd, "Development of a compton imager based on bars of scintillator," *Nucl. Instrum. Meth. Phys. Res. A*, vol. 767, pp. 397–406, 2014.
[3] G. F. Knoll, "Radiation spectroscopy with scintillators," *Radiation Detection and Measurement*, 4th Danvers, MA, USA: Wiley, 2010, pp. 359–361, ch. 10, sec. C.1.
[4] J. A. Nelder, and R. Mead, "A simplex method for function minimization," *J. Computers*, vol. 7, pp. 308–313, 1965.